



Systematic identification of allosteric effectors in *Escherichia coli* metabolism

Christoph Heinrich Gruber^{a,b} , Elad Noor^{a,c} , Marieke Francisca Buffing^{a,b}, and Uwe Sauer^{a,1}

Affiliations are included on p. 10.

Edited by Markus Ralser, Charité–Universitätsmedizin Berlin, Berlin, Germany; received November 14, 2024; accepted February 4, 2025 by Editorial Board Member Thomas J. Silhavy

Recent physical binding screens suggest that protein–metabolite interactions are more extensive than previously recognized. To elucidate the functional relevance of these interactions, we developed a mass spectrometry–based screening method for higher throughput *in vitro* enzyme assays. By systematically quantifying the effects of 79 metabolites on the activity of 20 central *Escherichia coli* enzymes, we not only assess functional relevance but also gauge the depth of the current understanding of regulatory interactions within one of the best-characterized networks. Our identification of 50 inhibitors and 14 activators not only expands the range of known input signals but also uncovers novel regulatory logic. For instance, we observed that AMP inhibits malic enzyme to safeguard the cyclic operation of the tricarboxylic acid cycle, and erythrose-4-phosphate inhibits 6-phosphogluconate dehydrogenase to redirect flux from the pentose phosphate pathway into the Entner–Doudoroff pathway. Discrepancies between our standardized assays and existing database entries suggest that many previously reported interactions might occur only under specific, often nonphysiological conditions. Our dataset represents a systematically determined functional protein–metabolite interaction network, establishing a baseline for allosteric regulation in central metabolism. These results enhance our understanding of the regulatory logic governing metabolic processes and underscore its significance in cellular adaptation and growth.

protein–metabolite interactions | allosteric regulation | metabolism | metabolomics | microbiology

Cells modulate their metabolic activity by adjusting enzyme levels through transcriptional or translational regulation, as well as rapidly altering enzymatic activity through posttranslational modifications or noncovalent binding of metabolites (1, 2). Direct translation of intracellular metabolite concentrations into metabolic responses enables swift adaptation to environmental changes and maintenance of homeostasis by interfering with binding of substrates to enzymes or allosteric modulation. The best-understood metabolite regulation is allosteric feedback inhibition in amino acid and nucleotide biosynthesis (3) and rapid reversal of pathway fluxes such as changing from glycolysis to gluconeogenesis (3, 4). Currently, databases contain approximately 1500 regulatory enzyme–metabolite interactions for *Escherichia coli* (5–7), the vast majority of which are not well understood in terms of their role in coordinating metabolism.

For decades, research on regulatory enzyme–metabolite interactions relied primarily on *in vitro* enzymology, totaling the equivalent of an estimated 9,000 person years of experimental work (8), but recent systematic physical interaction studies suggest that this interaction space might be much larger (9–12). Chemoproteomic mapping of ten glycolytic metabolites revealed almost 2,500 interactions with more than 900 target proteins in human cells (13). Two recent investigations of physical protein–metabolite interactions more than doubled the number of known interactions in *E. coli*'s central metabolism (14, 15), underscoring that the extent of allosteric regulation in even this well-studied network is still far from complete. A trivial explanation may be that *in vitro* studies typically report only a small set of regulators that were intuitively selected (1). With negative results rarely being reported, it is impossible to know how much of the possible interaction space has been probed so far. Moreover, assay conditions such as temperature, pH, and buffer composition usually optimize enzymatic activity rather than mimic physiological conditions (16), contesting whether all reported interactions matter *in vivo*. Conversely, systematic physical interaction studies lack functional context and display low overlap between studies (14, 15), leaving the true scope of regulatory enzyme–metabolite interactions uncertain. Comprehensive inquiries into their functional implications are hampered by the inability of present methods to simultaneously investigate a wide array of

Significance

Physical binding of metabolites to proteins is crucial for virtually every biological process; however, functional relevance is known for only very few of these interactions. Here, we develop a mass spectrometry-based approach to elucidate functional relevance of metabolite binding to enzymes. By testing 1,600 metabolite–enzyme combinations within central metabolism of the bacterium *Escherichia coli*, we present a systematically identified functional protein–metabolite interaction network. Despite central metabolism being one of the best-characterized molecular networks, we doubled the known regulatory interactions and provide evidence that many existing database entries lack physiological relevance. Several of these newly identified allosteric interactions reveal novel regulatory logic of some of the most fundamental metabolic pathways.

Author contributions: C.H.G., M.F.B., and U.S. designed research; C.H.G. performed research; C.H.G. and E.N. analyzed data; and C.H.G. and U.S. wrote the paper.

The authors declare no competing interest.

This article is a PNAS Direct Submission. M.R. is a guest editor invited by the Editorial Board.

Copyright © 2025 the Author(s). Published by PNAS. This article is distributed under [Creative Commons Attribution-NonCommercial-NoDerivatives License 4.0 \(CC BY-NC-ND\)](#).

¹To whom correspondence may be addressed. Email: sauer@ethz.ch.

This article contains supporting information online at <https://www.pnas.org/lookup/suppl/doi:10.1073/pnas.2423767122/-DCSupplemental>.

Published March 6, 2025.

interactions with both appropriate throughput and physiological relevance (17).

To gauge the depth of our current knowledge, we systematically mapped out functional enzyme regulation through metabolite binding in *E. coli*'s central metabolism, presumably one of the best-characterized systems. Our approach involved devising a screening pipeline for in vitro enzyme assays based on high-throughput mass-spectrometry (MS). This approach enabled systematic examination of potential regulatory interactions between 79 metabolites and 20 purified enzymes in standardized assays. At a 5% false-positive rate, we recovered most well-characterized interactions, questioned the in vivo relevance of several previously reported interactions, and newly identified 50 inhibitors and 14 activators. The outcome represents a systematically inferred network of functional enzyme regulation via metabolite binding in any organism.

Results

High-Throughput In Vitro Enzyme Assays in Standardized Conditions. We systematically investigated enzyme regulation via noncovalent metabolite-binding in *E. coli*'s central metabolism, focusing on major isoforms of monomeric and homomultimeric enzymes with commercially available substrates and cofactors. Excluding isomerases because identical reactant masses preclude MS analysis by flow injection (18), we selected 25 enzymes meeting these criteria and purified them via His-tag affinity purification from the ASKA strain library (19). However, five enzymes (FbaA, GapA, Mdh, Pgk, and Pps) could not be adequately purified using higher-throughput methods or were catalytically inactive ([Dataset S1](#)).

We systematically tested 79 endogenous metabolites, including central metabolites, cofactors, nucleotides, and global regulators ([Dataset S2](#)). This set included 57 previously reported enzyme-metabolite interactions affecting enzyme activity. Our method involved measuring enzymatic progress curves in the presence and absence of these potential effector molecules. To efficiently manage the time-resolved combinations of 20 enzymes with 79 metabolites in two biological and two technical replicates, we took advantage of high-throughput flow injection analysis (FIA) MS (18), a nontargeted metabolomics method. This allows direct detection of substrate depletion and product accumulation in reactions without the need for a second reaction generating optically detectable molecules, which potentially confounds interpretation.

To standardize single enzyme reaction monitoring, we used MS-compatible buffer conditions and metabolite concentrations suitable for detecting activators and inhibitors, mimicking in vivo conditions without introducing potentially confounding factors. All enzyme assays were conducted at 37 °C and pH 7.5 in 10 mM HEPES buffer. Metal cofactors were provided in excess to mitigate the risk of false positives due to metabolite-cofactors interactions. All substrates were supplied at 1 mM, exceeding most reported K_M values in central metabolism ([SI Appendix, Fig. S1](#)), mimicking typical cellular substrate concentrations that are usually about 10-fold higher than enzyme K_M -values (20). Monitoring entire progress curves instead of just initial velocities captured enzymatic velocity across a wide range of substrate and product concentrations in each assay. Each potential effector was tested at 5 mM, a concentration surpassing reported in vivo steady-state concentrations for nearly all tested metabolites (20–22) ([SI Appendix, Fig. S2](#)). In each 96-well microtiter plate assay, we tested the 79 potential effector metabolites and controls without effector or to exclude effects of salts or metal ions that are often part of commercially acquired metabolites (e.g. sodium or potassium salt hydrates; [Dataset S2](#)). Aliquots were collected and quenched with

–20 °C methanol at eight exponentially spaced timepoints (default: 0, 2, 4, 8, 16, 32, 64, and 128 min), aiming to cover a wide range of turnovers and enable detection of early activator effects while allowing reactions to approach equilibrium. Each assay was performed in at least two replicates that were measured twice in technical replicates using FIA-MS (Fig. 1A).

An automated custom-built analysis pipeline was set up to analyze MS time-course data for 1,580 enzyme-metabolite combinations and controls. Beyond published processing of FIA data (18), this included normalizing ion counts to the total ion count to correct for variations in injection volumes and filtering faulty injections or highly variable assays. For each enzyme, we extracted timeseries of two to four substrate and product ions (deprotonated, $[M-H^-]$). The pipeline identified the most reliable reactants for each enzyme based on the SD of replicates for reactants with redundant information and fitting enzymatic progress curves, ensuring high-quality data for analysis. Fig. 1 B–D illustrates resulting timeseries for the reactants of 6-phosphogluconate dehydrogenase (Gnd) assays, visually displaying the impact of added effectors on the reaction velocity. Based on chemical properties that cause different degrees of ion suppression, raw progress curves expectedly exhibited various degrees of signal suppression upon addition of potential effectors because they compete for ionization with the reactants (Fig. 1B).

Our method bypasses the need for time-consuming calibration curves or liquid chromatography to avoid ion suppression by scaling ion counts within each assay from start to end points. Due to the constancy of reaction equilibrium despite changes in enzyme velocity, we can scale least-squares fits based on an analytical solution to the reactant concentration over time for enzymatic reactions with Haldane kinetics (also known as reversible Michaelis–Menten; see *Materials and Methods* section titled “*Functions Used for Fitting Enzymatic Progress Curves*”). Instead of solely focusing on best-fit areas under the curve (AUC), we broadened our analysis by resampling mean and SD of each of the eight timepoints 200 times for each eligible ion, individually fitting and scaling them, thus encompassing the entire potential AUC range (Fig. 1C). When comparing scaled and fitted progress curves obtained via FIA-MS with classical photometer assay results from a similar setup, such as inhibition of Gnd by erythrose-4-phosphate (E4P) or 2-dehydro-3-deoxy-phosphogluconate (kgpd), we found qualitative agreement (Fig. 1E). This method not only streamlines measurements but also showcases qualitative consistency between our FIA-MS approach and established photometric assays.

To systematically assess effector function and gauge their impact on the activity of enzymes with varying progress curve shapes, we related observed AUC differences to estimated activity changes. Our curve-fitting model not only facilitated precise quantification of AUC but also was founded in enzyme kinetics, allowing us to simulate how changes in kinetic parameters would alter progress curves. For each enzyme, we applied our curve-fitting model to the overlaid progress curves from all control assays (i.e., those conducted without effectors) to obtain the best-fit parameters. With all other parameters fixed, we varied the k_{cat} parameter (via the β parameter, as described in the Methods section) to simulate new progress curves. While effectors can influence k_{cat} , K_M , or both—depending on their mechanism of action—we relied on changes in k_{cat} as a conceptual proxy. The relationship between changes in k_{cat} and the AUC of simulated progress curves allowed us to translate progress curve areas in all other assays to estimated fold-changes in these parameters and, thereby, enzymatic activity (Fig. 1D). The final score for each enzyme-effector combination was calculated as the \log_2 -fold activity change at the first quartile across fits from eligible reactants, indicating that 75% of the datapoints had equal

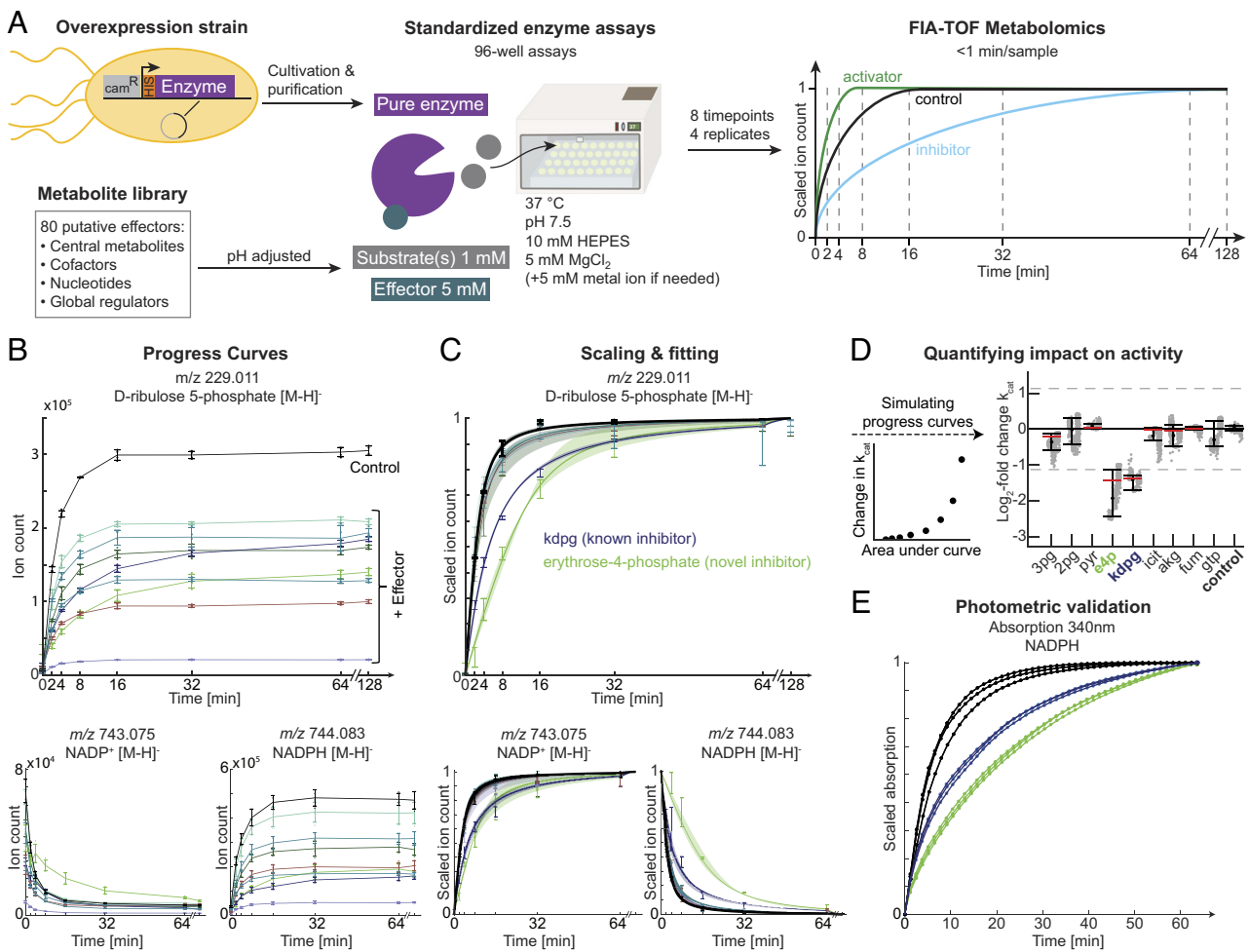


Fig. 1. High-throughput in vitro screening for enzyme activity effectors. (A) Experimental setup. His-tagged enzymes purified from an overexpression library were screened in microtiter plate assays under standardized conditions with 1 mM reactants and 5 mM potential effectors. In each assay, aliquots were quenched at eight timepoints (dashed lines) and metabolite ions detected with untargeted high-throughput flow-injection time-of-flight (FIA-TOF) MS. (B–D) Data analysis, exemplarily shown for the substrates (NADP⁺ [M-H]⁻) and products (D-ribulose-5-phosphate [M-H]⁻; NADPH [M-H]⁻) of 6-phosphogluconate dehydrogenase (Gnd). The acquired progress curves depicting product accumulation or substrate depletion with and without potential effectors including 2-dehydro-3-deoxy-phosphogluconate (kdpG) and erythrose-4-phosphate (e4p) (B) were rescaled to a range of 0 (start) and 1 (equilibrium). These scaled curves were then fitted based on an analytical solution to enzymatic progress curves with Haldane kinetics in a bootstrapping approach involving resampling the mean and SD of each timepoint, then fitting and scaling the curves for each resample (C). Error bars depict SD of acquired ion counts at each timepoint, and shaded areas represent the 95% CI derived from the bootstrapped population of fits. By fitting control assays and simulating progress curves with changes in the k_{cat} parameter, the relationship between the area of progress curves and k_{cat} was determined and then used as a proxy to quantify the impact of each tested effector on enzyme activity (D). Error bars correspond to 95% CI of fits in the MS-based assays and red lines show the 1st quartile; i.e., 75% of datapoints show an activity change larger than this value. (E) Comparison of scaled progress curves obtained in the MS-based screen versus those obtained via an NADPH-based photometric readout, exemplarily illustrated for the effects of e4p and kdpG on Gnd.

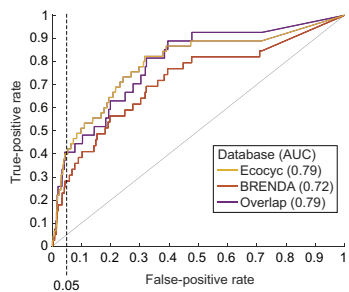
or higher changes. Notably, varying scoring metrics had minimal impact on results (*SI Appendix*, Fig. S3). This scoring system provided a quantifiable ranking for inhibitors and activators, enabling systematic comparison across all assays (*SI Appendix*, Fig. S4). Out of the 1,580 enzyme–effector combinations tested, 1,381 were deemed reliable based on technical criteria, which included meeting quality standards for ion traces, ensuring that tested metabolites were not the main reactants of the enzyme, confirming no precipitation events, and ruling out any influence of salts in the metabolite mix on enzymatic activity.

MS-Based Screening of Regulatory Enzyme–Metabolite Interactions and Photometric Validation Experiments. To identify regulatory events among the 1,381 reliably tested enzyme–effector pairs, we matched our ranked table (Dataset S3) against 57 previously reported regulatory combinations in the Ecocyc and BRENDA databases. Using receiver operating characteristic analysis, we determined a scoring threshold for our ranked table by assessing the database overlap with the percentage of assays

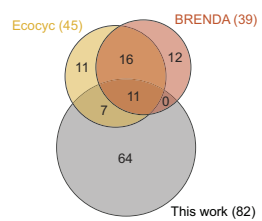
identified as hit at various scoring thresholds. The analysis revealed an AUC of 0.79 for Ecocyc and 0.71 for BRENDA (Fig. 2*A*). At a false-positive rate below 5% (scoring threshold: 1.131), the overlap with reported interactions was 40% for Ecocyc and 28% for BRENDA (Fig. 2*B*).

At a false-positive rate of 4.2% for Ecocyc and 4.8% for Brenda, we found 50 new inhibiting and 14 activating interactions, 25% of which exhibited strong effects, i.e., 12 inhibitors and five activators changed enzyme activity more than fourfold (Fig. 2*E* and *F*). This effectively doubled the number of known functional interactions in our tested combinations. Surprisingly, around 60% of previously reported interactions in Ecocyc and 69% including BRENDA could not be recovered. Even with a much lower threshold that would threefold increase false-positives, still 53% of literature entries from the databases would be missed (Fig. 2*C* and *D*). While some reported interactions were only slightly below the threshold, the vast majority were assigned a low score that cannot be explained by the chosen threshold. This discrepancy suggests either a large fraction of false-negatives, and potentially

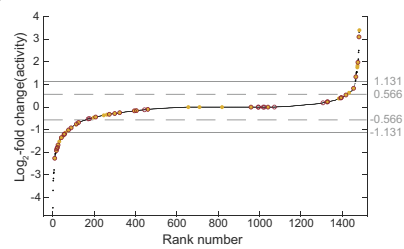
A



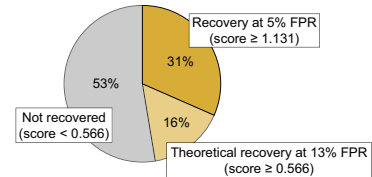
B



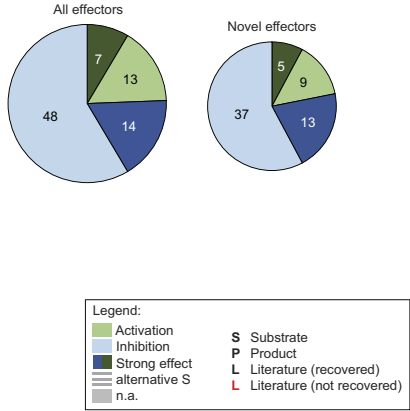
C



D



E



F

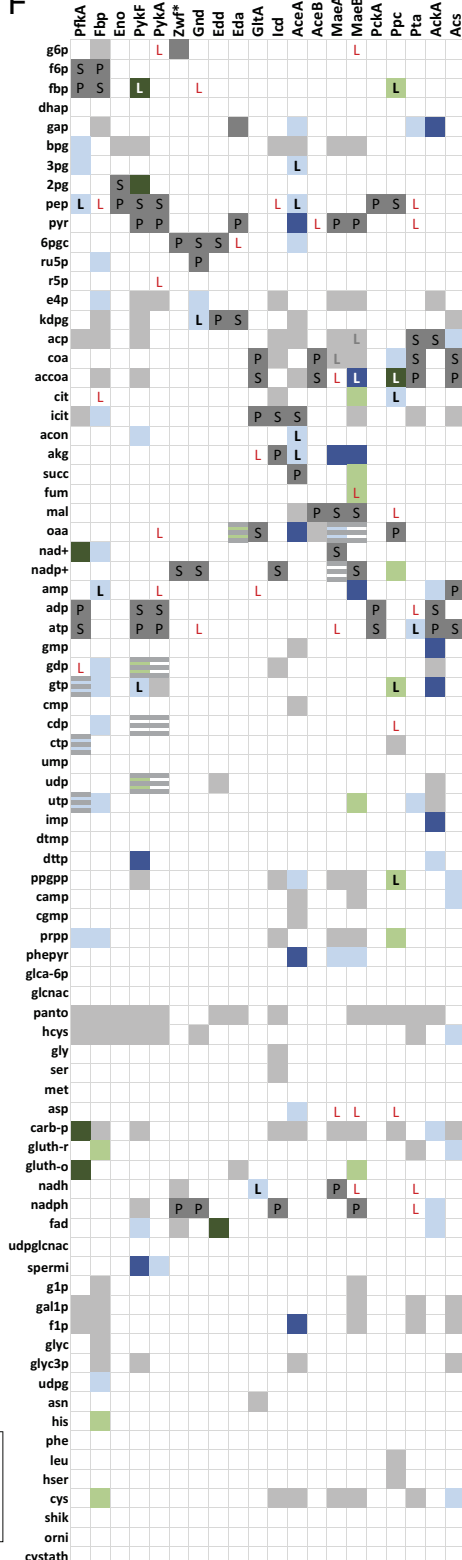


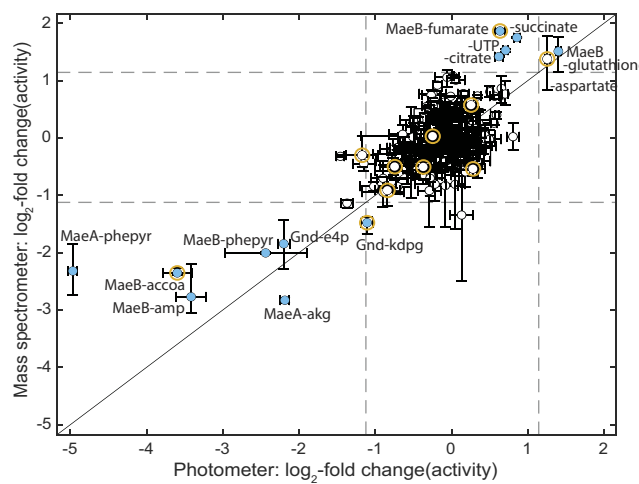
Fig. 2. Newly identified enzymatic activity effectors in *E. coli* central metabolism. (A) Receiver-operator characteristics curves for the obtained scores based on Ecocyc, BRENDA, or their overlap as true-positives. The vertical dashed line marks the 5% false-positive rate cutoff. (B) Overlap of identified effectors at a false-positive rate of 5% with reported cases in the Ecocyc and BRENDA databases. (C) Ranking of activity-based scores obtained in the MS screen (small black dots). Reported cases in Ecocyc and BRENDA are highlighted with yellow dots and red circles, respectively. Gray lines represent the chosen cutoff at 5% false-positive rate (score > 1.131) as well as a lower cutoff (score > 0.566) that would correspond to a 14% false-positive rate. (D) Impact of chosen threshold score on the recovery of known enzyme-effector interactions from BRENDA and Ecocyc. (E) Distribution of strong effects (score > 2.0) for inhibitors and activators (score > 1.131, 5% false-positive rate) among all identified effectors (Left) and among all novel effectors (Right). (F) Impact of 79 metabolites on the in vitro activity of 20 central enzymes in *E. coli*. Recovery of Ecocyc published effectors is indicated by the character L. The Zwf assays were recorded only photometrically (*). Means and errors of the underlying data are visualized in *SI Appendix*, Fig. S9 and listed in Dataset S3.

false-positives, in our MS-based assays, or that some database entries are based on weak evidence or are not reproducible in our conditions.

To benchmark the capability of our MS approach to identify regulatory interactions, we performed classical photometric assays based on NAD(P)H absorption spectra with all 79 tested metabolites on a subset of four selected enzymes—Gnd, isocitrate dehydrogenase (Icd), and the NAD- and NADP-dependent MaeA and

MaeB. These redox enzymes were chosen because their products NADH and NADPH can be directly quantified photometrically without coupled enzyme reactions and also covered varying confidence levels and hit counts in our MS screen. Conditions and analysis of progress curves were identical to the MS screen, except increasing the buffer to 100 mM HEPES to rule out pH or ionic strength effects. We considered both strong (\log_2 -fold change > 1.131, identical to cutoff at 5% FPR in MS approach) and weak

A



B

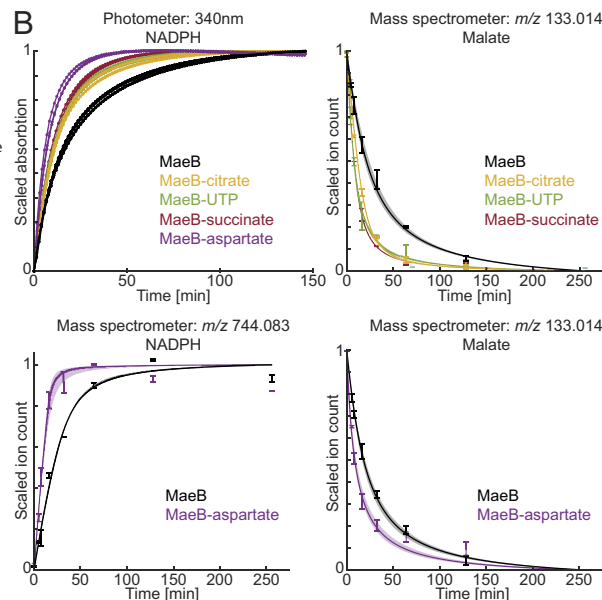


Fig. 3. Photometric validation of identified enzyme effectors. (A) Correlation of \log_2 -fold activity changes obtained via photometric and MS-based experiments for the redox enzymes MaeA, MaeB, 6-phosphogluconate dehydrogenase, and isocitrate dehydrogenase. Datapoints correspond to the mean and errors bars indicate the quartiles of obtained activity changes. Enzyme–effector combinations considered to be a hit at a 5% false-discovery rate are marked in blue, all others are shown in white. Combinations reported in the Ecocyc database are circled in yellow. (B) Direct comparison of MaeB photometric and MS-based progress curves for a subset of effectors. In the MS-based analysis, enzyme activity in presence of succinate, citrate, and UTP was quantified based solely on malate depletion timeseries, while for aspartate both malate depletion and NADPH accumulation timeseries were eligible for analysis (Bottom). For photometric progress curves, the scaled time points of the timeseries are shown. For MS-based progress curves, error bars depict SD of acquired ion counts at each timepoint, and shaded areas represent the 95% CI derived from the bootstrapped population of fits.

(\log_2 -fold change > 0.566 , corresponding to 14% FPR in MS approach) effects on enzymatic activity to avoid bias toward stronger effectors.

All ten inhibitors and activators with high MS-based scores were also confirmed in the photometric assays (Fig. 3A and *SI Appendix*, Fig. S5). Among these, seven displayed strong effects in either approach, while the three MaeB activators succinate, UTP, and citrate activated only weakly in photometric assays (Fig. 3B). Notably, these MaeB MS hits were among the low confidence assays, involving only one informing reactant. Thus, both methods yielded highly comparable qualitative conclusions, providing evidence that the substantial number of newly identified hits truly modulate enzymatic activity and are not false positives.

After confirming that all newly predicted interactions affected enzyme activity, we investigated why many database interactions were not detected in the MS screen, i.e., were classified as false negatives. Among the twelve regulatory interactions listed for Gnd, Icd, MaeA, and MaeB, ten were not found in the MS screen. Of the two cases identified using photometry but not MS, the aspartate–MaeB interaction had a slightly below threshold MS-based score (score: 0.84), while showing an effect slightly above threshold in photometric assays (score: 1.21) (Fig. 3B), and the missed interaction between fructose-bisphosphate and Gnd was confirmed to result in weak inhibition photometrically (score: 0.96). The remaining eight reported cases, however, were neither confirmed by MS nor photometric assays. Therefore, in the case of this specific subset of redox enzymes, the inability to detect reported regulatory interactions was not a result of the measurement technique; rather, enzymatic activity remained unaffected under the tested conditions.

The literature evidence behind the eight unconfirmed cases varies. Conflicting evidence was reported for MaeA's inhibition by acetyl-CoA (23, 24). For some cases, like MaeA's inhibition by succinate, only weak effects (15% change in activity) were reported (25). Additionally, several regulatory effects with MaeA, such as inhibition by ATP and activation by aspartate, were reported in

the absence of the metal cofactors Mg^{2+} or Mn^{2+} (26), while we used saturating concentrations. Similar conditions applied to MaeB's interactions with fumarate and glucose-6-phosphate, where effects were solely seen in the absence of Mn^{2+} (23). When repeating our malic enzyme experiments using buffers without Mn^{2+} and low Mg^{2+} concentrations, we found nonspecific responses to most tested metabolites (*SI Appendix*, Fig. S6), most pronounced was inhibition through negatively charged metabolites such as triphosphates or citrate that presumably chelate limiting metal cofactors. Likewise, the reported Icd inhibition by phosphoenolpyruvate resulted presumably from low cofactor concentrations (27), since we observed chelation-based effects at 1 mM but not at 10 mM Mg^{2+} (*SI Appendix*, Fig. S7). This suggests that previously reported effects under cofactor-limiting conditions might not reflect specific regulation of an enzyme, but rather were the result of unspecific interactions between metabolite and metal cofactor.

Beyond weak effects and limiting cofactors, the large number of discrepancies between our standardized assays and original experiments that accumulated over decades could be due to side effects from coupled enzyme assays or test conditions that maximized enzyme activity rather than reflect intracellular physiology. For instance, activation of 6-phosphofructokinase 1 (PfkA) through GDP is strong at low pH but weak at physiological pH (28). Consequently, the low recovery of previously reported regulatory interactions does not seem to be attributed to our MS-based approach. Instead, many of these missed interactions might only occur under very specific, sometimes nonphysiological conditions. Orthogonal testing with classical photometric methods thus validated two main outcomes from our systematic MS-based screen: A large fraction of reported database interactions might not be relevant under standardized physiological conditions and the space of functional enzyme–metabolite interactions exceeds previous knowledge. The many newly identified interactions might simply not have been tested in the past because

most assays involved only few commonly tested cofactors and metabolites.

Landscape of Systematically Inferred Regulatory Enzyme-Metabolite Interactions in *E. coli*'s Central Metabolism. After confirming the validity of our results with the subset of four redox enzymes, we examined the entire landscape of systematically identified regulatory interactions. Inhibitors of enzymatic activity can either bind to an allosteric site, a regulatory site distinct from the active site, or compete with substrates for the active site due to their chemical similarity. Using Simcomp2 (29), we assessed the maximum chemical similarity between our newly identified inhibitors and the target enzyme's reactants. Around 70% of inhibitors had maximum similarities below 0.5, with

a third even lower than 0.25 (Fig. 4A). This absence of strong chemical similarity between the effectors and reactants precludes competitive binding and thus suggests that the identified regulatory interactions primarily involve allosteric mechanisms.

Among the tested metabolites, 30 did not affect any enzyme, while the remaining 49 metabolites affected one to three and GTP four enzymes (SI Appendix, Fig. S8). Central, redox, and nucleotide metabolites affected on average 1.2, 1.25, and 1.1 enzymes, respectively, whereas amino acids affected about 0.5 enzymes (Fig. 4B). This suggests that regulation of central metabolism mainly involves central and redox metabolites, alongside nucleotides and various cofactors. Rather than few metabolites controlling many enzymes, our findings show that most tested metabolites regulate few enzymes. Mapping regulatory interactions onto

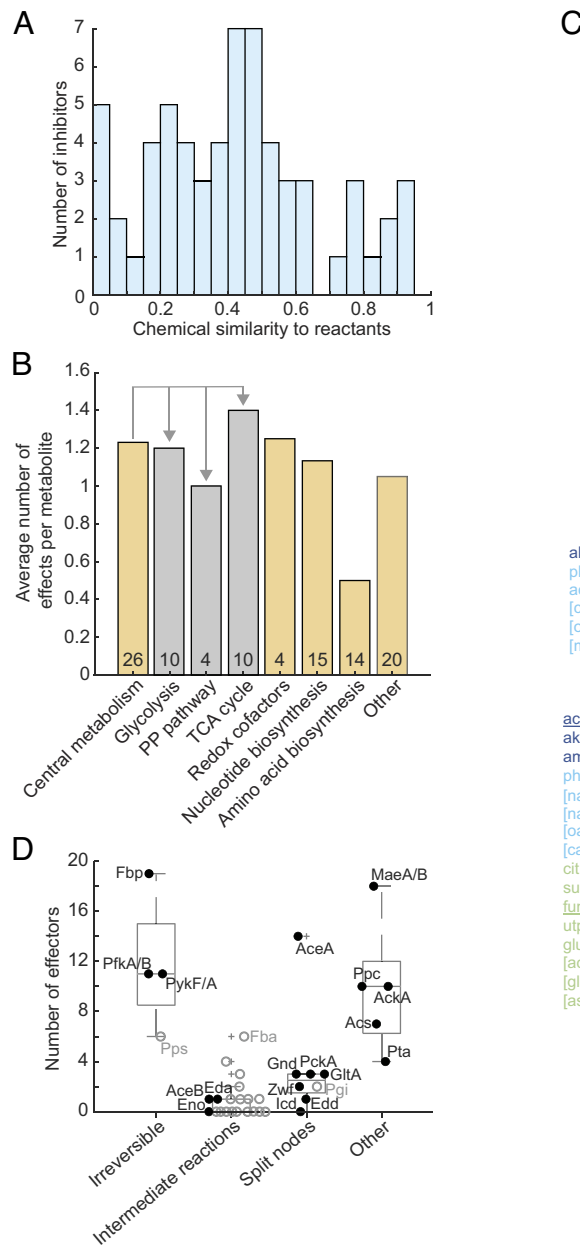


Fig. 4. Regulatory enzyme–effector interactions in *E. coli* central metabolism. (A) Maximum chemical similarity of identified inhibitors compared to the target enzyme's native substrates and products. (B) Average number of identified regulatory events per metabolite in different pathways. Numbers of tested pathway metabolites are given at the Bottom. The detailed interactions are shown in SI Appendix, Fig. S8. (C) Overview of inhibitors (blue) and activators (green) of the investigated enzymes (purple) in *E. coli* central metabolism. Strong effectors are in darker colors, previously reported ones are underscored. Brackets indicate effectors not tested or inconclusive in our screen but reported in at least two studies (5). Asterisks denote effectors with a borderline score (above 0.566; i.e. half of the chosen threshold corresponding to 14% false-positive rate) that were previously reported. The dataset is in Dataset S3. (D) Boxplots of the number of effectors per enzymatic reaction with different metabolic functions. Gray dots denote reactions with literature evidence (5) that were not tested in the screen.

central metabolism revealed little allosteric regulation in the pentose phosphate (PP) pathway and TCA cycle (Fig. 4C), consistent with previous observations (5–7, 14). Regulation hotspots with more than 10 effectors were the NADP⁺-dependent malic enzyme MaeB, the glycolytic pyruvate kinase (PykF), the gluconeogenic fructose-1,6-bisphosphatase (Fbp), the anaplerotic PEP carboxylase (Ppc), and isocitrate lyase (AceA) in the glyoxylate shunt. Expectedly, many effectors affected enzymes catalyzing irreversible reactions that determine flux direction (e.g., Fbp and PfkA) and anaplerotic reactions (e.g., Ppc and malic enzymes) (Fig. 4D). In contrast, intermediate reactions were generally targeted by few or no regulators. Apart from AceA, enzymes at split nodes were affected by few metabolites, such as Zwf catalyzing the first reaction of the PP pathway or GltA in the TCA cycle.

Several newly identified regulatory events echo established regulatory patterns. For instance, the irreversible glycolytic enzymes PfkA and PykF are active during glycolysis but must be inactivated during gluconeogenesis to avoid futile cycling and ATP waste (30). To achieve such a response, PfkA is inhibited by the lower glycolysis metabolite phosphoenolpyruvate and activated by ADP, a signal for low energy availability (3). Our findings show that also the lower glycolysis intermediates bisphosphoglycerate and 3-phosphoglycerate inhibit PfkA, while NAD⁺ strongly activates it, representing another signal of energy depletion (Fig. 5A). Similarly, in lower glycolysis, PykF is strongly activated by the upper glycolysis metabolite fructose-bisphosphate (31) and inhibited by succinyl-CoA and the nucleotide GTP that is intrinsically linked to cellular energy availability. Correspondingly, we found that the upstream glycolysis metabolite 2-phosphoglycerate strongly activates PykF. Moreover, the TCA cycle metabolite aconitate and the nucleotide (d)TTP were identified as strong inhibitors (Fig. 5A).

Other identified regulatory events revealed novel regulatory logic. For instance, the discovered feedback inhibition of Gnd by the PP pathway intermediate erythrose-4-phosphate (Fig. 5B). Presumably, the mechanism is through competitive inhibition given the moderate chemical similarity (0.5) of the effector to the reaction substrate 6-phosphogluconate and high chemical similarity (0.8) to its product ribulose-5-phosphate. While NADPH product inhibition was known to regulate the PP pathway at the initial enzyme Zwf (32), this finding adds a second control point further down the pathway.

Gnd plays a crucial role at the split node between the PP pathway and the Entner–Doudoroff pathway. This feedback inhibition of Gnd by erythrose-4-phosphate could redirect flux toward the Entner–Doudoroff pathway during high PP pathway flux when PP pathway intermediate levels are elevated. Previously thought to be mostly inactive in *E. coli*, the Entner–Doudoroff pathway was recently found to provide a selective advantage during rapid nutrient upshifts (33). The feedback inhibition of Gnd could be an underlying mechanism for this phenomenon.

Another case with novel regulatory logic is the NADP⁺-dependent malic enzyme MaeB that catalyzes the decarboxylation of malate to form pyruvate, thereby redirecting flux from the TCA cycle. It has important redox balancing functions and sits at a crucial metabolic crossroad, the PEP-pyruvate-oxaloacetate node that acts as a switch point for flux distribution (34). Beyond the known inhibition of MaeB by acetyl-CoA and oxaloacetate that initiate the TCA cycle (35, 36), we showed that not only rising levels of fumarate but also of citrate and succinate activate MaeB (Fig. 5C), suggesting that imbalanced or at capacity TCA cycle fluxes allosterically redirect flux from the cyclic operation to pyruvate. Conversely, we found AMP as a signal for low energy to be a potent inhibitor of MaeB (Fig. 5C), safeguarding energy production via the TCA cycle by preventing this flux diversion when energy is sparse. As an exception to the above MaeB activation through TCA cycle intermediates, both MaeB (Fig. 5C) and its isozyme MaeA (Fig. 4C) were strongly inhibited by another cycle intermediate: alpha-ketoglutarate. This metabolite is intricately related to nitrogen metabolism where the inhibition of MaeB may contribute to sustained TCA cycle fluxes under nitrogen limitation, where it accumulates up to 10 mM (37).

The three enzymes with the highest number of regulators were Fbp, AceA, and acetate kinase (AckA). In the case of Fbp, only one ion trace was informative (Fig. 2F) and the effects were comparatively small (*SI Appendix*, Fig. S4). As the first enzyme of the glyoxylate shunt, AceA was inhibited strongly by pyruvate and oxaloacetate (Fig. 5C) and more mildly by further intermediates of glycolysis and TCA cycle (Fig. 4C). High oxaloacetate levels indicate sufficient availability of carbon backbones in the TCA cycle and thus prevent further anaplerotic flux through the glyoxylate shunt to generate four carbon molecules during growth on acetate. The acetate-producing AckA was inhibited by AMP, GMP,

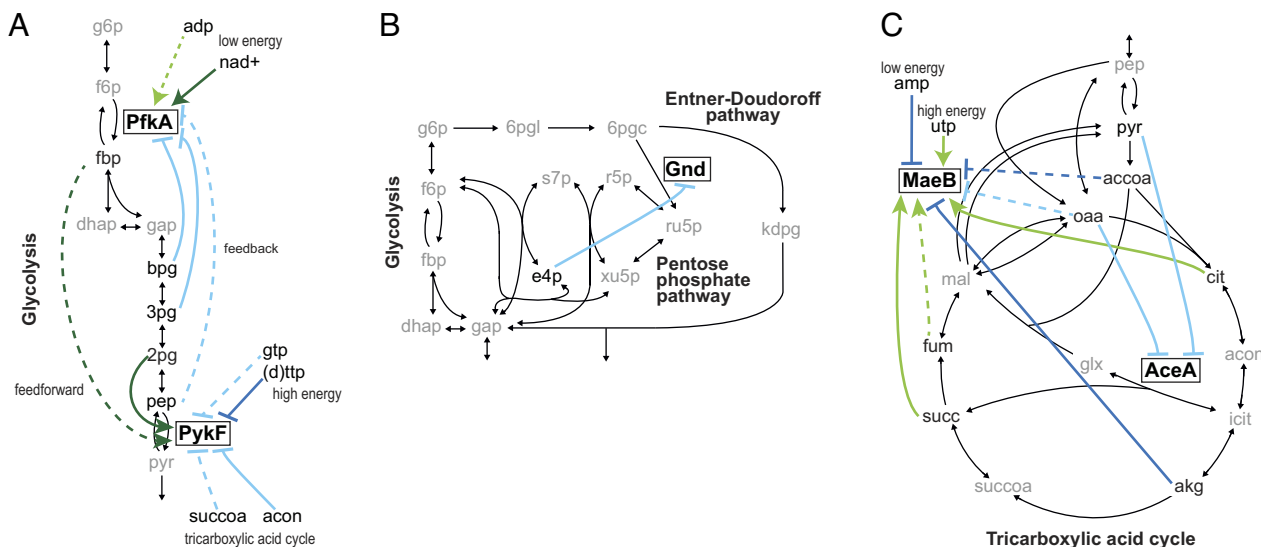


Fig. 5. Metabolic functions of identified enzyme-effector interactions. Established and novel regulation in glycolysis (A), at the decision point between the Entner–Doudoroff and pentose phosphate pathways (B), and in malic enzyme and the glyoxylate shunt (C). Dashed lines symbolize known and solid lines newly identified inhibition (blue) or activation (green).

and IMP. Given that overflow secretion of acetate generates less ATP than respiration, this newly identified inhibition constitutes a plausible mechanism to redirect flux toward respiration when the cellular energy state is low.

Discussion

The vast repository of meticulously conducted *in vitro* experiments (8) has been collected in databases (6, 7) and provides broad molecular knowledge on metabolism and its regulation. Yet, recent physical interaction screens suggested the spectrum of regulatory enzyme–metabolite interactions may be far more extensive than previously recognized (9–15). To assess the comprehensiveness of our knowledge of *E. coli*'s central metabolism, a screening method was employed to systematically map functional enzyme regulation. This approach yielded the identification of 50 inhibitors and 14 activators, more than doubling the previously documented regulatory effects of metabolites in this well-characterized network. In many cases, discovered regulatory interactions broaden the range of input signals that convey similar information. For instance, the activation of the NADP⁺-dependent enzyme MaeB through various TCA cycle intermediates. Similarly, the two irreversible enzymes in glycolysis are subject to feedback from several pathway intermediates and multiple metabolites that reflect the cellular energy status. This expanded information pool enables more adaptable and finely tuned metabolic responses.

A noteworthy example of previously unknown regulatory logic is the inhibition of MaeB through the low energy signal AMP, presumably safeguarding cyclic operation of the TCA cycle for efficient energy generation. At points where metabolic pathways diverge, known as flux split nodes, it is common for the first enzyme to be inhibited by the end products of that pathway. For instance, the enzyme Zwf in the PP pathway is inhibited by NADPH (38), while GltA in the TCA cycle is inhibited by NADH (39). However, little was known about negative feedback regulation at the split node between the PP and Entner–Doudoroff pathways. The here-described inhibition of Gnd through the PP pathway intermediate erythrose-4-phosphate provides such negative feedback. This regulation allows for the redirection of flux into the Entner–Doudoroff pathway, which exhibits a faster response time than glycolysis. This regulatory mechanism may be important for the recently reported rapid growth acceleration during carbon or nitrogen upshifts, which necessitates an expedited metabolic response (33). The regulatory effect may be ameliorated through phosphorylation of Gnd that is required for *in vivo* activity of the enzyme, potentially by promoting its interaction with metabolites or other proteins (40). Another case of end product inhibition was the effect of oxaloacetate on AceA that would reduce anaplerotic glyoxylate shunt flux, but may also play a role, jointly with pyruvate inhibition, for the PEP-glyoxylate cycle that is active under glucose limitation (41).

The disparities between our standardized assays and original experiments conducted over decades were rather surprising. Although the possibility of false negatives in our experiments cannot be ruled out, the extensive scope of these discrepancies, coupled with the successful validation of our findings using classical photometric assays for four redox enzymes, strongly indicates systematic issues. Examination of original experiments for the tested redox enzymes revealed that many effectors reported in present databases exhibit weak effects, were obtained under conditions of limiting cofactor concentrations, or employed test conditions that maximized enzyme activity rather than mimicking intracellular physiology. Additionally, confounding factors such as unintended side effects from coupled enzyme assays in classical

enzymology further contribute to the complexity of the situation. Nonetheless, it is reassuring to note that our screening process has successfully identified the most well-known and robust allosteric interactions. Notably, this includes the feedforward activation of PykF by fructose-bisphosphate (31) and the feedback inhibition of PfkA by phosphoenolpyruvate (42), both of which are crucial for regulating the switch between glycolysis and gluconeogenesis. Another prominent example is the ultrasensitive activation of Ppc by fructose-bisphosphate and acetyl-CoA which prevents futile cycling during gluconeogenesis and facilitates fast glucose import after periods of starvation (43).

Mass spectrometric approaches similar to the one presented here are broadly applicable to other enzymes and organisms. However, one limitation of FIA-MS is its inability to differentiate between reactants with identical masses, which excludes isomerases from the analysis. While we did not prioritize isomerases as key targets of metabolic regulation, incorporating chromatographic separation through LC-MS would enable discrimination of isomeric reactants (44, 45). This enhancement, however, would substantially reduce throughput. Likewise, we prioritized enzymes that are amenable to high-throughput purification. While specialized purification and assay protocols could enable the study of membrane-bound enzymes and complexes, this too would come at the cost of throughput.

Other limitations pertain to our analysis and fitting approach. Our primary objective was to determine whether an effect was occurring and to approximate its magnitude. This was achieved by comparing AUC values from progress curves of enzyme–metabolite pairs to simulations of how control assay AUCs change with alterations in k_{cat} . This process required scaling progress curves between the start and equilibrium points and assumed that effectors primarily impacted k_{cat} , regardless of their exact mechanisms. Moreover, bimolecular reactions were modeled under the assumption of reaction irreversibility, idealizing binding mechanisms, and identical substrate concentrations, among other factors (*SI Appendix*, Text S1). These simplifications facilitated the high-throughput nature of the study, but they may have limited the precision of the estimated changes. For instance, scaling progress curves between start and end points may have led to an underestimation of inhibitory potency in certain cases. Addressing these limitations would necessitate significantly more experiments for each enzyme–metabolite combination to achieve higher timepoint resolution and a broader range of tested conditions. Realistically, this would only be feasible for a very small subset of promising cases.

This systematic investigation of regulatory interactions in *E. coli* provides a baseline for allosteric regulation of central metabolism. It reveals regulation hotspots in central metabolism that are primarily controlled through central and redox metabolites. Rather than few metabolites controlling many enzymes, most tested metabolites regulated only few enzymes. Collectively, these findings enhance our understanding of the regulatory logic governing metabolic processes and highlight their importance in cellular adaptation and growth.

Materials and Methods

Enzyme Expression and Purification. All *E. coli* strains used in this study were obtained from the ASKA collection (19), an overexpression library with each strain containing an open reading frame of a gene from *E. coli* K-12 W3110. Cells were inoculated in a 1:100 dilution from 5 mL LB medium precultures to shake flasks with 200 mL LB medium (5 g/L yeast extract, 10 g/L tryptone, 10 g/L NaCl) supplemented with 100 µg/mL chloramphenicol (Sigma-Aldrich). Expression of the target protein was induced with 0.1 mM isopropyl β-D-1-thiogalactopyranoside and the cultures were grown for 16 h at 37 °C with shaking (300 rpm). Cells were

harvested by centrifugation (5,000 g and 4 °C for 20 min) and pellets were resuspended in lysis buffer containing bacterial protein extraction reagent (B-PER™, Thermo Scientific) supplemented with 500 mM NaCl, 20 mM imidazole, 1 mM MgCl₂, 0.2 mg/mL DNase I (Roche), 2 mg/mL lysozyme (Fluka), 4 mM phenylmethanesulfonyl fluoride and 10% glycerol. The suspension was shaken for 10 min at room temperature and then cell debris was pelleted via centrifugation (21,000 g at 4 °C for 45 min). The supernatant containing his-tagged soluble proteins was collected. His-tagged proteins were purified using His GraviTrap TALON gravity flow columns (GE Healthcare). After loading the supernatant to the column, it was washed twice with 10 mL buffer containing 20 mM NaPO₄, 0.5 M NaCl, 20 mM imidazole, and 10% (v/v) glycerol at pH 7.5. The bound protein was then eluted with 3 mL of a similar buffer containing 500 mM imidazole. The elution buffer containing the purified protein was exchanged with 5× enzyme buffer (50 mM HEPES, 25 mM MgCl₂, 5 mM additional metal cofactors if required, pH 7.5) using Zeba spin desalting columns with a 7 kDa cutoff. Protein purity was assessed by sodium dodecyl sulfate–polyacrylamide gel electrophoresis. Purified proteins were flash-frozen in liquid nitrogen and stored at –80 °C.

Effector Library Preparation. All metabolites, including substrates, cofactors, salt controls, and potential enzymatic effectors, were purchased with the highest purity available from Merck (Sigma-Aldrich) except for guanosine-3',5'-bispyrophosphate (ppGpp) and fructose-1-phosphate, obtained from Jena Bioscience and Santa Cruz Biotechnology, respectively. To maintain consistent pH during addition of potential effectors and avoid potential biases due to pH shifts when adding metabolites, as described in literature (46), all stock solutions of potential enzymatic effectors and all controls were prepared in 10 mM HEPES buffer and preadjusted to pH 7.5 using NaOH and HCl. The library included 79 potential effector metabolites, and every 12th sample served as a control without an effector. Additionally, controls containing salt and metal ions were included to account for potential effects of salts or metal ions, which are commonly present in commercially acquired metabolites (Dataset S2). Aliquots of this library were stored in 96-well plates at –80 °C.

Primary Screen: MS-Based Enzyme Activity Assays. Activity assays were conducted in a 96-well format within a heating chamber maintained at 37 °C. Assay buffers for each enzyme were freshly prepared and adjusted to pH 7.5. They contained 10 mM HEPES, 5 mM MgCl₂, and substrates and cofactors specific to each enzyme. Substrates and organic cofactors (e.g., NADH, NADPH) were each supplied at a final concentration of 1 mM. If required for enzymatic activity, an additional 5 mM of inorganic cofactors, such as MgCl₂ or MnCl₂, were included (Dataset S1). Each well of the 96-well plate received 88 μL of assay buffer and 11 μL of an effector or control solution from the previously prepared effector library. A pipetting robot was employed to ensure simultaneous initiation and sampling of all 96 assays. Before starting the reaction, a timepoint zero measurement was taken by withdrawing 9 μL of the reaction mixture from each well and mixing with 1 μL of 10 mM HEPES in 90 μL methanol precooled to –20 °C. The enzyme, previously stored in 5× enzyme buffer at –80 °C, was centrifuged at 20,000 g for 2 min at room temperature to remove precipitates, and then diluted to reach 1× enzyme buffer (10 mM HEPES, 5 mM MgCl₂, 5 mM additional metal cofactors if required, pH 7.5). A 10 μL aliquot of the enzyme at a concentration previously determined in preliminary tests (see below) was added to each well to start the reaction. At exponentially spaced time intervals (default: 2, 4, 8, 16, 32, 64, and 128 min), 10 μL samples were withdrawn and immediately mixed with 90 μL of precooled methanol provided in another 96-well plate, thereby denaturing the protein and quenching the enzymatic reaction. Plates containing methanol were precooled to –20 °C before sampling, kept on a cold metal rack during sampling, and subsequently stored at –80 °C. Each assay was performed in two experimental replicates.

Preliminary Tests: MS-Based Enzyme Activity Assays. Before conducting the main activity assays as described above, a preliminary experiment was carried out to determine an enzyme concentration that would achieve equilibrium within the experimental timeframe while the progress curve is effectively captured (SI Appendix, Fig. S10). To accomplish this, a twofold serial dilution of each enzyme was tested in the absence of effectors. These diluted enzyme samples were added to a 96-well plate in the same manner as the main assays, with 88 μL of assay buffer and 11 μL of assay buffer instead of an effector solution. Reactions were monitored at exponentially spaced time intervals (0, 2, 4, 8, 16, 32, 64, and 128 min) identical to the approach in the main activity assays. The samples were measured on a mass spectrometer as outlined below and the data from these

preliminary assays were analyzed to identify a suitable enzyme concentration for subsequent activity assays with effectors.

FIA-TOF MS. Enzyme assay samples were further diluted 1:1 in methanol before they were analyzed using a previously described untargeted metabolomics approach (18) utilizing a Gerstel MPS2 autosampler and an Agilent 6520 Q-TOF mass spectrometer. The flow rate was set to 150 μL/min with a mobile phase composed of isopropanol:water (60:40, v/v) and 5 mM ammonium fluoride at pH 9.0. Taurocholic acid and hexakis-phosphazine were supplemented for online mass axis correction. Measurements were conducted in negative ionization mode, with spectra recorded over a mass-to-charge ratio (m/z) range of 50 to 1,000, at a rate of 1.4 spectra/s in extended dynamic range mode (2 GHz EDR). For each sample, two technical replicates were measured. To minimize potential biases and temporal drifts associated with extended mass spectrometer operation, the assays for each enzyme were measured in two sequential batches. The units 1 to 4 of effectors and controls were measured, followed by a cleaning and recalibration of the mass spectrometer before measuring units 5 to 8 of effectors and controls (Dataset S2).

Processing Spectral Data of Enzymatic Progress Curves. Spectral raw data (47) were preprocessed and annotated using an in-house developed pipeline in Matlab (The MathWorks) as described previously (18). Annotation was performed using reference values from the KEGG database for *E. coli*, assuming simple deprotonation ([M–H][–]) and applying a mass tolerance of 0.005 Da. For each enzyme, timeseries data were extracted for its two to four substrate and product ions. To minimize artifacts, timeseries in which the ion count did not exceed a threshold of 5,000 were excluded. Faulty injections were identified by comparing the total ion count (TIC) of each sample to the median TIC of all samples that were part of the same effector or control condition tested on a given enzyme. Samples were excluded if their TIC deviated by more than 50% from the median TIC. To correct for variations in signal intensity and injection volumes, all ion counts were normalized to the median TIC across all samples measured for a given enzyme. Assays in which an effector was tested whose mass matches the ion of interest were excluded from further analysis. Following the application of these quality criteria, only assays with at least six out of eight time points remaining and including values for timepoints zero were retained for further analysis. Assays that did not meet these criteria were classified as inconclusive.

Analysis of Enzymatic Progress Curves. From the two to four reactants of each enzyme, each in theory holding the same information on enzymatic activity but with expected variance in data quality based on their chemical properties, we selected the reactants with the best-quality ion traces. To this end, a least-squares fit based on a time-course ODE solution based on Haldane kinetics (see below) was performed on each timeseries from control assays (i.e., assays without effector) and we selected the reactants that yielded the best R-squared values as well as those within 0.1 range of the best R-squared value. Borderline cases were resolved through visual inspection. For all ion traces of the remaining reactants, data from the two experimental and two technical replicates were lumped together, and mean and SD were calculated for each timepoint. Then bootstrapping was performed by resampling the mean of each timepoint 200 times based on their calculated SD assuming standard normal distribution. After each resampling, a least-squares fit with our fitting model based on Haldane kinetics (see below) was performed on the resampled timepoints, the resulting fit was scaled between 0 (start) and 1 (equilibrium), and its area under the curve (AUC) was calculated. Fits with an R-squared value below 0.7 were omitted from further analysis, and if 50% or more of the fits for a given assay were of poor quality, the assay was considered inconclusive. Remaining AUCs were translated to estimated changes in enzymatic activity by performing a least-squares fit with our fitting model based on Haldane kinetics to the overlaid progress curves of all control assays of an enzyme, i.e. all assays without added effectors. The resulting set of optimal parameters was fixed while varying the k_{cat} parameter to simulate new progress curves. These simulated progress curves functioned similarly to a calibration curve, establishing a relationship between changes in k_{cat} and their corresponding AUCs. This relationship was used to translate the progress curve areas in assays with effectors into estimates of enzymatic activity changes. For each enzyme–effector combination, the translated AUCs from all eligible reactants were pooled together to form a population. The final score was derived as the log2-fold activity change at the first quartile of this population. This ensured that 75% of the data points showed equal or greater activity changes, providing a relatively robust summary of effector influence that minimizes the impact of outliers or extreme

values. Other metrics based on population percentages were obtained in a similar manner, e.g. 95% CI used for scoring (*SI Appendix*, Fig. S3) correspond to 97.5% of data points showing equal or greater activity changes. Accordingly, 95% CI for visual representation of the bootstrapping approach (Figs. 1C and 3B) were calculated by sorting the AUCs from each bootstrapping fit and selecting the interval between the 2.5th and 97.5th percentiles. Note that the fitting of controls and translation of effector AUCs were performed separately for each measurement batch of an enzyme, with controls from units 1 to 4 used to translate effectors in those units, and controls from units 5 to 8 used similarly.

Validation Experiments: Spectrophotometric Enzyme Activity Assays.

Spectrophotometric assays were performed on four dehydrogenases (Gnd, Icd, MaeA, MaeB) measuring NADH or NADPH production via changes in absorbance at 340 nm. The experimental design and analysis followed the mass spectrometry approach with modifications to accommodate the photometric method. Assays were conducted in a 96-well format at 37 °C. Instead of a discontinuous sampling and quenching approach, photometric assays were performed continuously in three experimental replicates. 100 mM instead of 10 mM HEPES (pH 7.5) were used in the buffer. Absorbance at timepoint zero was measured by adding 180 µL of enzyme buffer to each well, followed by an absorption measurement. Then, 20 µL of enzyme were added and the plate was immediately transferred to the photometer preheated to 37 °C, while recording the time between the initiation of the reaction and the start of measurement. A least-squares fit with our fitting model based on Haldane kinetics was performed on each of the three replicates. The fit was scaled between 0 and 1, and AUC was calculated. Estimated activity changes were derived from the AUCs by fitting control assays and simulating changes in k_{cat} similar to the MS method. For each enzyme–effector combination, the first quartile was calculated as $\mu - 0.675\sigma$, where μ represents the mean and σ the SD of the three replicates.

Functions Used for Fitting Enzymatic Progress Curves. The function used to fit the time-dependent trajectory of accumulation of reaction products, $P(t)$, is based on the analytical solution to the ordinary differential equation system where the rate of the reaction is described by Haldane's rate law, sometimes referred to as reversible Michaelis–Menten rate law. The solution for a reaction with one substrate and one product is

$$P(t) = P(\infty) \cdot \left[1 - \frac{W_0(\omega e^\omega e^{-\beta t})}{W_0(\omega e^\omega)} \right],$$

1. K. Kochanowski, U. Sauer, E. Noor, Posttranslational regulation of microbial metabolism. *Curr. Opin. Microbiol.* **27**, 10–17 (2015).
2. D. Holbrook-Smith, J. Trouillon, U. Sauer, Metabolomics and microbial metabolism: Toward a systematic understanding. *Annu. Rev. Biophys.* **53**, 41–64 (2024).
3. V. Chubukov, L. Gerosa, K. Kochanowski, U. Sauer, Coordination of microbial metabolism. *Nat. Rev. Microbiol.* **12**, 327–340 (2014).
4. H. Link, K. Kochanowski, U. Sauer, Systematic identification of allosteric protein–metabolite interactions that control enzyme activity *in vivo*. *Nat. Biotechnol.* **31**, 357–361 (2013).
5. E. Reznik *et al.*, Genome-scale architecture of small molecule regulatory networks and the fundamental trade-off between regulation and enzymatic activity. *Cell Rep.* **20**, 2666–2677 (2017).
6. A. Chang *et al.*, BRENDA, the ELIXIR core data resource in 2021: New developments and updates. *Nucleic Acids Res.* **49**, D498–D508 (2021).
7. I. M. Keseler *et al.*, The EcoCyc database in 2021. *Front. Microbiol.* **12**, 711077 (2021).
8. M. T. Alam *et al.*, The self-inhibitory nature of metabolic networks and its alleviation through compartmentalization. *Nat. Commun.* **8**, 16018 (2017).
9. D. Veyel *et al.*, PROMIS, global analysis of PRotein–metabolite interactions using size separation in *Arabidopsis thaliana*. *J. Biol. Chem.* **293**, 12440–12453 (2018).
10. V. Cappelletti *et al.*, Dynamic 3D proteomes reveal protein functional alterations at high resolution in situ. *Cell* **184**, 545–559.e22 (2021).
11. M. M. Rinschen, J. Ivanisevic, M. Giera, G. Siuzdak, Identification of bioactive metabolites using activity metabolomics. *Nat. Rev. Mol. Cell Biol.* **20**, 353–367 (2019).
12. K. G. Hicks *et al.*, Protein–metabolite interactomics of carbohydrate metabolism reveal regulation of lactate dehydrogenase. *Science* **379**, 996–1003 (2023).
13. Y. Tian *et al.*, Chemoproteomic mapping of the glycolytic targetome in cancer cells. *Nat Chem Biol* **19**, 1480–1491 (2023).
14. M. Diether, Y. Nikolaev, F. H. Allain, U. Sauer, Systematic mapping of protein–metabolite interactions in central metabolism of *Escherichia coli*. *Mol. Syst. Biol.* **15**, e9008 (2019).
15. I. Piazza *et al.*, A map of protein–metabolite interactions reveals principles of chemical communication. *Cell* **172**, 358–372.e23 (2018).
16. H. Bisswanger, Enzyme assays. *Perspect. Sci.* **1**, 41–55 (2014).
17. P. Stincone, A. Naimi, A. J. Saviola, R. Reher, D. Petras, Decoding the molecular interplay in the central dogma: An overview of mass spectrometry-based methods to investigate protein–metabolite interactions. *Proteomics* **24**, 2200533 (2023).

where W_0 is the zeroth branch of the Lambert W function (i.e. the inverse function of ωe^ω) and $P(\infty)$ corresponds to the final equilibrium concentration of the product. We replaced physical parameters with effective ones used for fitting the function, namely $\omega \leftarrow P(\infty)/K_M^*$ and $\beta \leftarrow E k_{cat}^*/K_M^*$.

In the case of reactions with two substrates, in order to get an analytical solution, we assume that both substrates start with the same initial concentration, and that their binding to the enzyme follow an idealized binding mechanism, where there is no enzyme–substrate complex with a single substrate but instead both substrates simultaneously bind to the enzyme. In this case, the solution will be

$$P(t) = P(\infty) \cdot \left[1 - \frac{\sqrt{(\beta t + \omega^{-1} - \omega)^2 + 4} - (\beta t + \omega^{-1} - \omega)}{2\omega} \right],$$

As in the case of one substrate, $P(\infty)$ corresponds to the final equilibrium concentration of the product. ω and β are the fitting parameters.

For an in-depth explanation and full mathematical derivations of these formulae, see *SI Appendix*, Text S1.

Chemical Similarity Computation. Chemical similarities between effector metabolites and enzyme substrates and products were calculated via the web-based tool Simcomp2 (29) using the mode “local.”

Data, Materials, and Software Availability. Raw mass spectrometry was made available through <http://massive.ucsd.edu> and can be found via <https://massive.ucsd.edu/ProteoSAFe/dataset.jsp?accession=MSV000096497> (47). Raw photometry and (pre)processed mass spectrometry data are published via [10.5281/zenodo.14226986](https://zenodo.14226986); this repository holds resulting MATLAB files after peak picking, annotation, and quantification of all measured ions (48). Additionally, it holds tables with the relevant information, i.e., substrate and product ion traces of each enzyme, sorted by tested metabolite, timepoints, and replicates. The computational pipeline used for both mass spectrometry and photometer data, as well as code for performing key analyses and creating corresponding figures was made public on <https://github.com/gruberchristoph/MSprogresscurves> (49).

Author affiliations: ^aDepartment of Biology, Institute of Molecular Systems Biology, ETH Zürich, Zürich 8093, Switzerland; ^bLife Science Zurich PhD Program on Systems Biology, Zurich 8057, Switzerland; and ^cDepartment of Plant and Environmental Sciences, Weizmann Institute of Science, Rehovot 76100, Israel

18. T. Fuhrer, D. Heer, B. Begemann, N. Zamboni, High-throughput, accurate mass metabolome profiling of cellular extracts by flow injection–time-of-flight mass spectrometry. *Anal. Chem.* **83**, 7074–7080 (2011).
19. M. Kitagawa *et al.*, Complete set of ORF clones of *Escherichia coli* ASKA library (A Complete Set of *E. coli* K-12 ORF Archive): Unique resources for biological research. *DNA Res.* **12**, 291–299 (2005).
20. B. D. Bennett *et al.*, Absolute metabolite concentrations and implied enzyme active site occupancy in *Escherichia coli*. *Nat. Chem. Biol.* **5**, 593–599 (2009).
21. K. Kochanowski *et al.*, Few regulatory metabolites coordinate expression of central metabolic genes in *Escherichia coli*. *Mol. Syst. Biol.* **13**, 903 (2017).
22. L. Gerosa *et al.*, Pseudo-transition analysis identifies the key regulators of dynamic metabolic adaptations from steady-state data. *Cell Syst.* **1**, 270–282 (2015).
23. F. P. Bologna, C. S. Andreo, M. F. Drincovich, *Escherichia coli* malic enzymes: Two isoforms with substantial differences in kinetic properties, metabolic regulation, and structure. *J. Bacteriol.* **189**, 5937–5946 (2007).
24. R. A. Cook, Distinct metal cofactor-induced conformational states in the NAD-specific malic enzyme of *Escherichia coli* as revealed by proteolysis studies. *Biochim. Biophys. Acta* **749**, 198–203 (1983).
25. M. Iwakura, M. Tokushige, H. Katsuki, S. Muramatsu, Studies on regulatory functions of malic enzymes. *J. Biochem.* **83**, 1387–1394 (1978).
26. J. A. Milne, R. A. Cook, Role of metal cofactors in enzyme regulation. Differences in the regulatory properties of the *Escherichia coli* nicotinamide adenine dinucleotide specific malic enzyme depending on whether magnesium(2+) or manganese(2+) serves as divalent cation. *Biochemistry* **18**, 3604–3610 (1979).
27. T. Ogawa *et al.*, Role of phosphoenolpyruvate in the NADP-isocitrate dehydrogenase and isocitrate lyase reaction in *Escherichia coli*. *J. Bacteriol.* **189**, 1176–1178 (2007).
28. D. Deville-Bonne, F. Bourgoin, J. R. Garel, pH dependence of the kinetic properties of allosteric phosphofructokinase from *Escherichia coli*. *Biochemistry* **30**, 5750–5754 (1991).
29. M. Hattori, N. Tanaka, M. Kanehisa, S. Goto, SIMCOMP/SUBCOMP: Chemical structure search servers for network analyses. *Nucleic Acids Res.* **38**, W652–W656 (2010).
30. M. Basan *et al.*, A universal trade-off between growth and lag in fluctuating environments. *Nature* **584**, 470–474 (2020).
31. G. Valentini *et al.*, The allosteric regulation of pyruvate kinase. *J. Biol. Chem.* **275**, 18145–18152 (2000).
32. D. Christodoulou *et al.*, Reserve flux capacity in the pentose phosphate pathway enables *Escherichia coli*'s rapid response to oxidative stress. *Cell Syst.* **6**, 569–578.e7 (2018).

33. R. C. Law, G. Nurwono, J. O. Park, A parallel glycolysis provides a selective advantage through rapid growth acceleration. *Nat. Chem. Biol.* **20**, 314–322 (2023).
34. U. Sauer, B. J. Eikmanns, The PEP-pyruvate-oxaloacetate node as the switch point for carbon flux distribution in bacteria. *FEMS Microbiol. Rev.* **29**, 765–794 (2005).
35. B. D. Sanwal, R. Smando, Malic enzyme of *Escherichia coli*. Diversity of the effectors controlling enzyme activity. *J. Biol. Chem.* **244**, 1817–1823 (1969).
36. L. F. Huergo *et al.*, The NADP-dependent malic enzyme MaeB is a central metabolic hub controlled by the acetyl-CoA to CoASH ratio. *Biochim. Biophys. Acta* **1868**, 140462 (2020).
37. J. Yuan *et al.*, Metabolomics-driven quantitative analysis of ammonia assimilation in *E. coli*. *Mol. Syst. Biol.* **5**, 302 (2009).
38. K. Olavarria, D. Valdés, R. Cabrera, The cofactor preference of glucose-6-phosphate dehydrogenase from *Escherichia coli*: Modeling the physiological production of reduced cofactors. *FEBS J.* **279**, 2296–2309 (2012).
39. H. W. Duckworth *et al.*, Enzyme-substrate complexes of allosteric citrate synthase: Evidence for a novel intermediate in substrate binding. *Biochim. Biophys. Acta* **1834**, 2546–2553 (2013).
40. E. Schastnaya *et al.*, Extensive regulation of enzyme activity by phosphorylation in *Escherichia coli*. *Nat. Commun.* **12**, 5650 (2021).
41. E. Fischer, U. Sauer, A novel metabolic cycle catalyzes glucose oxidation and anaplerosis in hungry *Escherichia coli**. *J. Biol. Chem.* **278**, 46446–46451 (2003).
42. D. Blangy, H. Buc, J. Monod, Kinetics of the allosteric interactions of phosphofructokinase from *Escherichia coli*. *J. Mol. Biol.* **31**, 13–35 (1968).
43. Y.-F. Xu, D. Amador-Noguez, M. L. Reaves, X.-J. Feng, J. D. Rabinowitz, Ultrasensitive regulation of anapleurosis via allosteric activation of PEP carboxylase. *Nat. Chem. Biol.* **8**, 562–568 (2012).
44. W.-C. Yang *et al.*, Simultaneous quantification of metabolites involved in central carbon and energy metabolism using reversed-phase liquid chromatography–mass spectrometry and *in vitro* 13C labeling. *Anal. Chem.* **80**, 9508–9516 (2008).
45. K. Serafimov, M. Lämmerhofer, Comprehensive coverage of glycolysis and pentose phosphate metabolic pathways by isomer-selective accurate targeted hydrophilic interaction liquid chromatography–tandem mass spectrometry assay. *Anal. Chem.* **96**, 17271–17279 (2024).
46. D. Šimčková, P. Heneberg, Identification of alkaline pH optimum of human glucokinase because of ATP-mediated bias correction in outcomes of enzyme assays. *Sci. Rep.* **9**, 11422 (2019).
47. C. H. Gruber, Systematic identification of allosteric effectors in *Escherichia coli* metabolism. MassIVE. <https://massive.ucsd.edu/ProteoSAFe/dataset.jsp?accession=MSV000096497>. Accessed 19 February 2025.
48. C. H. Gruber, MATLAB results files of MS-based analysis–Systematic identification of allosteric effectors in *Escherichia coli* metabolism. Zenodo. <https://zenodo.org/records/14226986>. Accessed 19 February 2025.
49. C. H. Gruber, E. Noor, MSprogresscurves. GitHub. <https://github.com/gruberchristoph/MSprogresscurves>. Accessed 19 February 2025.